energies

MDPI

Article

Direct Comparison of Immersion and Cold-Plate Based Cooling for Automotive Li-Ion Battery Modules

Prahit Dubey *, Gautam Pulugundla and A. K. Srouji

Romeo Power Technology, 4380 Ayers Ave, Vernon, CA 90058, USA; gautam@romeopower.com (G.P.); ak@romeopower.com (A.K.S.)
* Correspondence: prahit.dubey@gmail.com

Abstract: The current paper evaluates the thermal performance of immersion cooling for an Electric Vehicle (EV) battery module comprised of NCA-chemistry based cylindrical 21700 format Lithium-ion cells. Efficacy of immersion cooling in improving maximum cell temperature, cell's temperature gradient, cell-to-cell temperature differential, and pressure drop in the module are investigated by direct comparison with a cold-plate-cooled battery module. Parametric analyses are performed at different module discharge C-rates and coolant flow rates to understand the sensitivity of each cooling strategy to important system performance parameters. The entire numerical analysis is performed using a validated 3*D* time-accurate Computational Fluid Dynamics (CFD) methodology in STAR-CCM+. Results demonstrate that immersion cooling due its higher thermal conductance leads to a lower maximum cell temperature and lower temperature gradients within the cells at high discharge rates. However, a higher rate of heat rejection and poor thermal properties of the dielectric liquid results in a much higher temperature non-uniformity across the module. At lower discharge rates, the two cooling methods show similar thermal performance. Additionally, owing to the lower viscosity and density of the considered dielectric liquid, an immersion-cooled battery module performs significantly better than the cold-plate-cooled module in terms of both coolant pressure drop.

Keywords: Li-ion battery module; NCA 21700 cylindrical cells; thermal management system (TMS); dielectric liquid; immersion cooling; cold-plate cooling; computational fluid dynamics (CFD) simulations

check for updates

Citation: Dubey, P.; Pulugundla, G.; Srouji, A.K. Direct Comparison of Immersion and Cold-Plate based Cooling for Automotive Li-Ion Battery Modules. *Energies* **2021**, *14*, 1259. https://doi.org/10.3390/en14051259

Academic Editor: Danny Pudjianto

Received: 24 January 2021
Accepted: 17 February 2021
Published: 25 February 2021

Publisher's Note: MDPI stays neutral with regard to jurisdictional claims in published maps and institutional affiliations.

Copyright: © 2021 by the authors. Licensee MDPI, Basel, Switzerland. This article is an open access article distributed under the terms and conditions of the Creative Commons Attribution (CC BY) license (https://creativecommons.org/licenses/by/4.0/).

1. Introduction

Driven by a strong motivation to reduce air pollution and carbon emissions, several countries around the world have actively supported the technological development and improved sales of Battery Electric Vehicles (BEV) and Plug-in Hybrid Electric Vehicles (PHEV) through government incentives such as direct funding and customer subsidies [1]. In the year 2019 alone, sales of global passenger light-duty electric automobiles crossed 7.2 million [1]. With sustained government policies and support, this number is projected to increase several-fold to 119 million by 2030 [2]. However, this strong growth in Electric Vehicle (EV) sales does not have to be limited to these projected numbers. By addressing certain critical technological challenges, a further expansion of the EV market can be achieved in the next 10 years. Some of these challenges include development of Lithium-ion (Li-ion) batteries having higher energy density, longer cycle life, higher discharge performance, and finally having fast charging capabilities, thereby alleviating any concerns of long wait times at charging stations [3]. Thus, development of battery packs capable of operating under higher charge/discharge C-rates, without significant capacity degradation, is of high significance.

One of the critical battery pack components needed to achieve all the aforementioned targets is an efficient Thermal Management System (TMS). In particular, TMS plays an

important role in achieving longer battery life under aggressive discharge or charge conditions, while preventing extreme thermal events during operation [4]. It has been shown previously that higher battery temperature rapidly degrades the performance [5] and accelerates cell ageing [6,7]. In addition, for battery packs that operate under aggressive duty cycles or C-rates, such as a high-performance BEV [8,9] or a PHEV [10,11], it is crucial that the TMS and its underlying cooling mechanism are capable of dissipating the high heat generated during module operation and keeping the cell temperatures within a reasonable limit. Along with the reduction in maximum cell temperatures, it is also important to keep the temperature gradients within a cell to a minimum. Under a high temperature gradient, a Li-ion cell behaves as if it is operating under a higher than average temperature [12]. Existing literature has demonstrated that, in addition to negatively impacting the cycle life [13], a high temperature gradient across a Li-ion cell results in inhomogeneous current density distribution and state-of-charge (SOC) causing localized ageing throughout the cell [14].

Over the past few years, many EV manufacturers have actively adapted TMS based on liquid cooling technology [15], which mainly consists of a heat exchanger either in the form of a bottom cold-plate [16,17] or a circumferential serpentine manifold [18] as used by Tesla Inc. (San Carlos, CA, USA). All these cooling systems have provisions for coolant inlet and outlet ports, temperature sensors, and thermal interface materials. These heat exchangers are often metallic and therefore achieve contact with the cells through a dielectric coating or adhesive usually having lower thermal conductivity. Especially in these bottom-cooled scenarios, only a small area of the cell is available for heat transfer to the coolant. This results in a higher thermal resistance for the heat transfer from the cells to the coolant and thus higher maximum temperatures and gradients. It is worth noting that, for pouch cells, cold plates can be affixed to the two sides of the the cell. However, for cylindrical cells, cold plate cooling options are limited as the electrical conductors are typically routed on the top of the cell [16,17].

To overcome these inherent disadvantages of bottom cold-plate cooling for cylindrical cells, some researchers in the past have proposed, among other techniques, a novel immersion cooling strategy for battery systems. Kim and Pesaran [19] showed that immersion cooling provides improved heat transfer compared to a water-jacket based cooling, but at the expense of higher pressure drop. Patil et al. [20] investigated mineral oil based cooling for pouch cells at 6 W/cell and noted that dielectric cooling is a feasible option for improving thermal performance. Deng et al. [21] extended the use of oil based immersion cooling further and discussed that higher viscosity of oil results in a limited improvement of 1.5–3 times in heat transfer at the same pressure drop compared to air cooling. More recently, experimental and numerical work performed by Sundin and Sponholtz [22], Pulugundla et al. [7], and Patil et al. [23] showed encouraging thermal performance of immersion cooling. Specifically, Sundin and Sponholtz [22] conducted an experimental investigation showing lower temperatures of a 68 Ah prismatic Li-ion cell under their charge/discharge cycle and directly compared the thermal performance of immersion cooling against that of air cooling. During their study, the peak current was only limited to 0.55 C. Pulugundla et al. [7] evaluated the efficacy of immersion cooling through experimental and numerical analysis based on a single cylindrical lithium-nickel-cobalt-aluminum oxide (NCA) Li-ion Cell of 21700 form factor. They demonstrated that at a 3 C continuous discharge from a cell voltage of 4.1 V to 3 V, temperature of the cell and the temperature gradient along the vertical direction (from the top to the bottom of the cell) is reduced considerably compared to the cold-plate based cooling due to the direct contact of the dielectric cooling liquid with the cell. Patil et al. [23] investigated experimentally and numerically the performance of dielectric immersion cooling strategy on a single pouch cell and a 50 V battery pack comprised of 14 pouch cells. They evaluated the effectiveness of various combinations of immersion cooling and air cooling with respect to maximum cell temperatures. Among other observations, they concluded that forced immersion cooling together with tab air cooling reduced maximum cell temperature by 46.3% at a 3 C discharge rate.

As discussed above, a few studies in the past have analyzed the thermal performance of immersion cooling for battery thermal management. However, the comparison of its performance for cylindrical cells has often been limited to and with air cooling rather than any type of liquid cooling, especially cold-plate cooling. Thus, it is important to present a direct comparison between the thermal performance of the two types of cooling methods to facilitate the discussion on the limitation and advantages of one cooling method over the other for battery modules. In addition, previous studies available in the literature for cylindrical Li-ion cells are primarily based on single-cell level investigations. While these studies have presented results for maximum cell temperature, and other parameters of interest for an automotive battery pack such as the temperature gradients, they have not discussed or presented the important cell-to-cell temperature differential across a battery module or a pack. Thus, it is crucial to extend the single-cell level immersion-cooling models to an automotive battery module and explore the resulting temperature and flow distribution inside it. Such an investigation should be able to reveal the advantages and the underlying limitations of immersion cooling at the battery module level when compared to a cold-plate based cooling, especially those that have not been evident through single-cell level studies. Keeping the above discussion in mind, the present work aims to achieve the following:

1. Evaluation of the thermal performance of an immersion-cooled automotive Li-Ion battery module comprised of cylindrical 21700 format lithium-nickel-cobalt-aluminum oxide (NCA) cells, under aggressive continuous discharge C-rates with special focus on:
   (a) Analyzing the effect of C-rates, coolant flow rates on the cell temperatures, thermal conductance, and pressure drop inside an immersion-cooled battery module.
   (b) Identifying disadvantages of immersion cooling, if any, through analysis of temperature or flow distribution in the battery module for the considered coolant flow and C-rates.
2. Evaluation of the thermal performance of a cold-plate-cooled automotive Li-Ion battery module with identical cells and geometrical layout as the immersion-cooled battery module. This will enable us to obtain a direct comparison of the thermal performance of immersion-cooled and cold-plate-cooled battery modules.

For both battery modules, this study utilizes a validated time-accurate three-dimensional (3*D*) Computational Fluid Dynamics (CFD) model in STAR-CCM+ with a state of charge (SOC) dependent heat load from the Li-ion cells.

The present research work is organized as follows: Section 2 introduces the geometric details of immersion-cooled and cold-plate-cooled battery modules, material properties, mathematical models with the associated numerical method, and numerical uncertainty analysis through verification (Section 2.7.1) and validation procedures (Section 2.7.2). Results from direct comparison of immersion cooling and cold-plate cooling for a reference case at a coolant flow rate of 6 LPM and module discharge rate of 2*C* are presented in Section 3.1. In Section 3.2, the effect of module discharge C-rates of 0.5 C, 1 C, 2 C, and 3 C at a fixed coolant flow rate of 6 LPM on thermal performance of immersion-cooled and cold-plate modules is analyzed. In Section 3.3, a direct comparison of the two cooling strategies is performed by analyzing the effect of coolant flow rates of 2 LPM, 4 LPM, and 6 LPM at a fixed module discharge rate of 2 C on the module thermal performance. The results and discussion in Section 3 are finally followed by conclusions in Section 4.

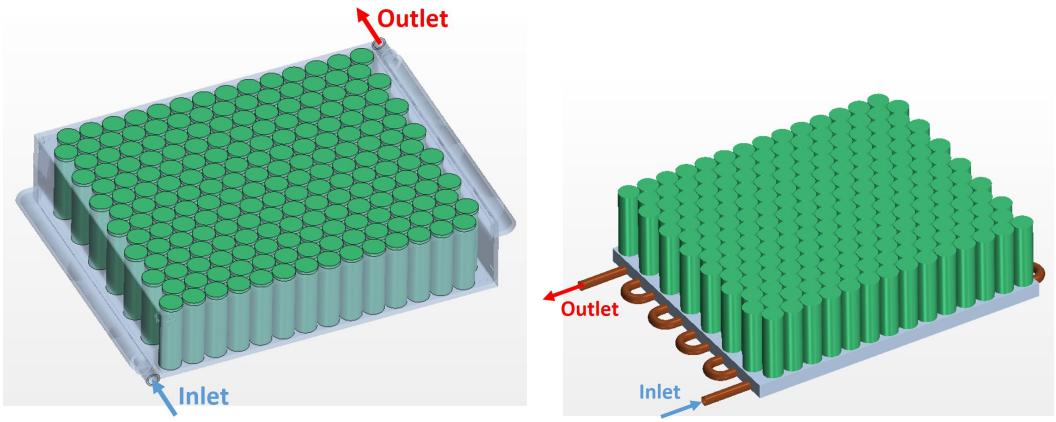
2. Methodology

To study and compare the effectiveness of the two Li-ion cooling strategies—namely, immersion cooling and cold-plate cooling—two automotive battery modules each consisting of geometrically identical staggered arrangement of 196 cylindrical lithium-nickel-cobalt-aluminum oxide (NCA) chemistry based Li-ion cells of 21700 form-factor (Figure 1)

are considered. Details for the geometric and numerical setup are described in the following sub-sections.

2.1. Geometry Description

In the case of immersion-cooled battery module, the Li-ion cells are contained within an enclosure made of poly-carbonate with outer dimensions of 330 mm × 280 mm × 73 mm. The module enclosure has one inlet and one outlet port for the flow of a dielectric coolant (Figure 1a). The entire battery module is assumed to be tightly sealed such that there is no coolant leak. All the Li-ion cells are exposed to the dielectric liquid to almost 90% of their height (63 mm). The height of 63 mm is chosen to ensure that there is enough space at the top of the cells to achieve a leak-proof sealing of the dielectric liquid within the enclosure. For the cold-plate-cooled module, the base of the cells are affixed to the top surface of an aluminum cold-plate (Figure 1b) of size 320 mm × 270 mm × 15 mm. Coolant flows through a copper serpentine tube of internal diameter 7 mm embedded in an aluminum block. Like the immersion-cooled module, there is an inlet and an outlet face on the copper tubes for the coolant flow.



(**a**) (**b**)

Figure 1. CAD model employed for the numerical simulations of (**a**) immersion cooling, and (**b**) cold-plate cooling.

2.2. Material Properties

The dielectric coolant used for immersion cooling is a commercially available hydrofluoroether from 3M™ called NOVEC™ 7500 [24]. The coolant used in cold-plate cooling is a 50-50 mix of water and ethylene glycol (WEG) [25,26]. The material properties of both dielectric coolant and WEG 50/50 are shown in Tables 1 and 2, respectively. Table 3 presents the material properties of the solids used in the two simulations [27]. Here, ρ, μ, k, and C_p represent density, dynamic viscosity, thermal conductivity, and specific heat, respectively.

Table 1. Temperature dependent thermo-physical properties of dielectric coolant used for immersion cooling of the battery module [24].

Property	Dielectric Coolant (3M™ NOVEC™)
ρ [kg/m^3]	$-2.0845 \times T$[°C] $+ 1665.8$; 20 °C $\leq T \leq$ 70 °C
μ [Pa sec]	$1 \times 10^{-7} \times T^2$[°C] $- 3 \times 10{-}5 \times T$[°C] $+ 0.0018$; 20 °C $\leq T \leq$ 70 °C
C_p [J/(kg K)]	$1.4982 \times T$[°C] $+ 1091$; 20 °C $\leq T \leq$ 70 °C
k [W/(m K)]	$4 \times 10^{-7} \times T^2$[°C] $- 0.0002 \times T$[°C] $+ 0.069$; 20 °C $\leq T \leq$ 70 °C

Table 2. Temperature dependent thermo-physical properties of 50/50 ethylene glycol (EG)–water used for cold-plate cooling of the battery module [25,26].

Property	50/50 EG–Water Mixture
ρ [kg/m^3]	$-0.615 \times T$[K] $+ 1259.5$; 293.15 K $\leq T \leq$ 353.15 K
μ [Pa sec]	$2.48 \times 10^{-8} \times T^3$[K] $+ 2.47 \times 10^{-5} \times T^2$[K] $- 8.22 \times 10{-}3 \times T$[K] $+ 0.92$; 277.15 K $\leq T \leq$ 345.15 K
C_p [J/(kg K)]	$3.06 \times T$[K] $+ 2574.8$; 293.15 K $\leq T \leq$ 353.15 K
k [W/(m K)]	$-2 \times 10^{-7} \times T^3$[K] $+ 0.0002 \times T^2$[K] $- 0.048 \times T$[K] $+ 5.38$; 293.15 K $\leq T \leq$ 343.15 K

Table 3. Thermo-physical properties of solid regions used for immersion and cold-plate cooling [27].

Property	Immersion Cooling Enclosure	Copper Tube (Cold-Plate)	Aluminum Plate (Cold-Plate)
ρ [kg/m^3]	1200	8940	2710
C_p [J/(kg K)]	1200	386	900
k [W/(m K)]	0.2	398	200

2.3. Mathematical Model

Computational domains in the simulation of each battery module (Figure 1) consist of several different regions, depending on the difference in applied physics and material properties. For the immersion-cooled battery module, these regions are non-metallic enclosure, cylindrical cells, and dielectric coolant. For the cold-plate cooling cases, the regions are copper tubing, aluminum block, cylindrical cells, 50/50 EG/water, and ambient air. For the numerical analysis of both these systems, the following assumptions are considered:

- The coolants (dielectric and 50/50 EG/water mixture) are incompressible and Newtonian.
- The effect of buoyancy in the coolant flow is neglected.
- The effective heat transfer modes inside the entire system are convection and conduction. The influence of radiation is neglected.
- Heat generation by the Li-ion cells is only through irreversible Ohmic heating (5). The influence of reversible entropic heat generation is neglected.

Based on the above assumptions, the governing $3D$ partial differential equations (Figure 1) reduce to the following form:

Coolant (c):

$$\nabla \cdot \vec{u}_c = 0, \tag{1}$$

$$\rho_c \frac{\partial \vec{u}_c}{\partial t} + (\vec{u}_c \cdot \nabla)\vec{u}_c = -\nabla p + \mu_c \nabla^2 \vec{u}_c + \rho_c \vec{g}, \tag{2}$$

$$\frac{\partial T_c}{\partial t} + (\vec{u}_c \cdot \nabla)T = \frac{\kappa_c}{\rho_c C_{p_c}} \nabla^2 T_c. \tag{3}$$

Li-ion cells (cell):

$$\frac{\partial T_{cell}}{\partial t} = \frac{\kappa_{cell}}{\rho_{cell} C_{p_{cell}}} \nabla^2 T_{cell} + q_{cell}, \tag{4}$$

$$\dot{q}_{cell} = i^2 R. \tag{5}$$

Cold-plate or immersion enclosure (cp):

$$\frac{\partial T_{cp}}{\partial t} = \frac{\kappa_{cp}}{\rho_{cp} C_{p_{cp}}} \nabla^2 T_{cp}. \tag{6}$$

Ambient Air(a):

$$\frac{\partial \rho_a}{\partial t} + \nabla \cdot (\rho_a \vec{u}_a) = 0, \tag{7}$$

$$\frac{D(\rho_a \vec{u}_a)}{Dt} = -\nabla p + \mu_a \left[\nabla^2 \vec{u}_a + \frac{1}{3} \nabla (\nabla \cdot \vec{u}_a) \right] + \rho_a \vec{g}, \tag{8}$$

$$\frac{D(\rho_a T_a)}{Dt} = \frac{\kappa_a}{C_{p_a}} \nabla^2 T_a, \tag{9}$$

$$\rho_a = \frac{p_a}{R_s T_a}. \tag{10}$$

In the above equations, $\nabla \cdot$ is divergence operator, ∇ is gradient operator, $\vec{u}$ is velocity in m/s, T is temperature in K, p is pressure in pa, $\vec{g}$ is acceleration due to gravity in m/s^2, $\kappa/\rho C_p$ is thermal diffusivity in m^2/s, μ is dynamic viscosity in pa s, and R_s is gas constant in $J/(kg\,K)$.

2.4. Numerical Method

In this section, the details of the numerical method employed for the $3D$ time-accurate numerical simulations using the commercial CFD software package STAR-CCM+ [27] are presented. The numerical approach employed in STAR-CCM+ is based on a finite-volume discretization of the governing Equations (1)–(10) using an algebraic multigrid based iterative solver that is second order accurate in space and first order accurate in time. The solver employs a Semi-Implicit Method for Pressure Linked Equation (SIMPLE) algorithm for pressure velocity coupling [28]. This algorithm is based on a predictor–corrector approach, which employs the relationship between velocity and pressure corrections to enforce mass conservation and to obtain the pressure field. The turbulent flow behavior is captured using an eddy-viscosity based Unsteady Reynolds Averaged Navier Stokes (URANS) approach. Finally, to improve the numerical stability of the simulations, an initial time step of 0.1 second is employed, which is then gradually increased to 1 second as the simulation progresses. Temperature and flow variables are converged to within 0.05% at each of the time steps to ensure overall time accuracy of the transient numerical results.

2.5. Initial and Boundary Conditions

The current section describes the initial and boundary conditions that are employed to compute the flow and temperature fields for all considered numerical simulations. At the start of the solution, the temperature for all the computational domains (solids, fluids) is initialized to 25 °C. For the parametric simulations, we consider three different flow rates of 2 LPM, 4 LPM, and 6 LPM for both immersion and cold-plate cooling cases. Here, LPM denotes the flow rate in units of liters-per-minute of coolant. The velocity boundary condition is derived from these flow rates and the inlet port cross-sectional area, and applied using a plug-profile at the inlet flow boundary. A mean shear is setup by no-slip boundary conditions for the solid walls. Temperature of the coolant at the inlet of the modules in both cases is kept at 25 °C. The pressure outlet condition is used at the outlet of the coolant flow boundary [15,27]. For all the outer surfaces of the ambient air domain, a Heat Transfer Coefficient (HTC) of $5\,W/m^2K$ at a reference temperature of 25 °C is applied in the form of a convection boundary condition. Equation (5) is utilized to estimate the heat generation for both the immersion-cooled and cold-plate-cooled modules. The transient behavior of heat generation based on State of Charge (100% to 0%) is also considered in the estimation of heat generation. For the parametric simulations, we consider four different

module discharge C-rates of 0.5 C, 1 C, 2 C, and 3 C for both immersion and cold-plate cooling cases. The estimated heat generation is then applied as a volumetric heat source in the Equation (4) for each 21700 Li-ion cells considered in the simulations (Figure 2).

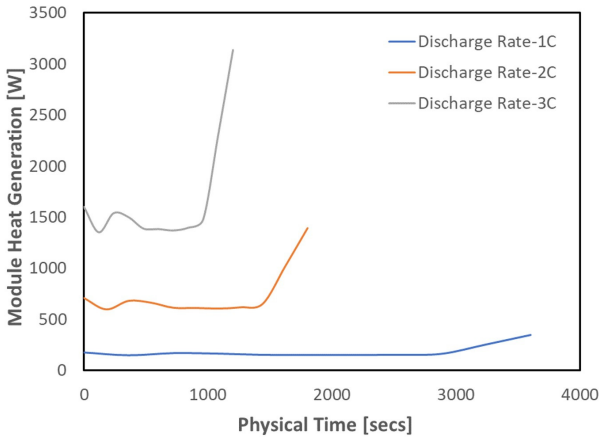


Figure 2. Module heat generation as a function of time when the module discharges from SOC of 100% to 0% at different C-rates.

A total of 14 cases are simulated as listed in Table 4 considering the available computational resources. As it will become clear in the following sections, the specific values of the discharge C-rates and coolant flow rates listed in Table 4 facilitates a thorough direct comparison of the two cooling strategies. Furthermore, the highest discharge limit of 3 C is set by the cell specific operational limit. The highest coolant flow rate of 6 LPM is determined considering the limitation of the available test equipment. Unless otherwise stated, the results shown in Section 3 correspond to those at the final time-step when the module has completed discharged and the cells have reached an SOC of 0%. The total discharge time of the module depends on the C-rate. However, it must be emphasized here that, if the polarization effects of the Li-ion cells are taken into account, the total module discharge time at a given C-rate would be lower than that considered in the numerical simulations.

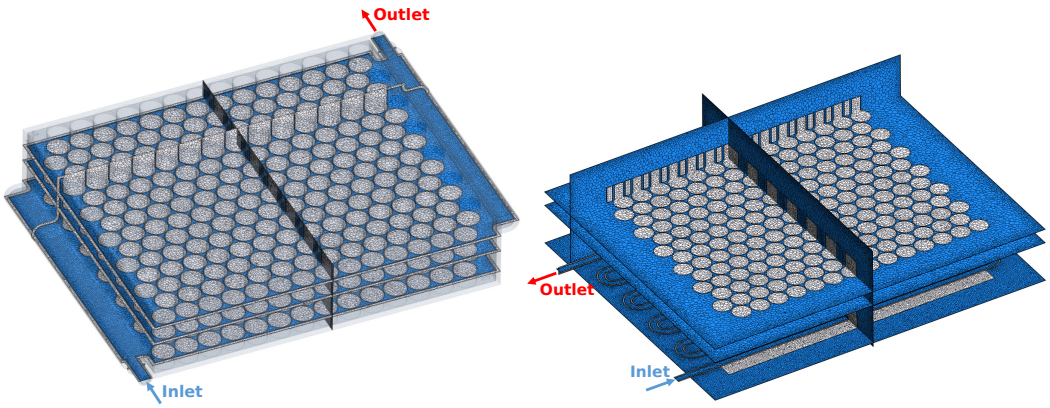
Table 4. Simulation matrix with coolant flow rate and battery module discharge conditions.

Case #	Cooling Strategy	Coolant Flow Rate [LPM]	Discharge C-Rate	Discharge Time [secs]
1	Immersion	6	0.5	7200
2	Immersion	6	1	3600
3	Immersion	6	2	1800
4	Immersion	6	2	1800
5	Immersion	6	2	1800
6	Immersion	6	3	1200
7	Immersion	2	2	1800
8	Immersion	4	2	1800
9	Cold-Plate	6	0.5	7200
10	Cold-Plate	6	1	3600
11	Cold-Plate	6	2	1800
12	Cold-Plate	6	3	1200
13	Cold-Plate	2	2	1800
14	Cold-Plate	4	2	1800

Note: Cases 3–5 are part of a grid independence study (Section 2.7). Therefore, they feature the same parameters but three different grid sizes.

2.6. Grid Generation

One of the most important considerations for performing accurate numerical simulations is the grid resolution employed to discretize the computational domains. Therefore, high quality grids capable of resolving both the temperature and flow gradients accurately are generated for both immersion-cooled and cold-plate-cooled battery modules. Tables 5 and 6 show the total number of computational elements in each solid and fluid domain considered in the simulations. In this work, we use the built-in grid generator in STAR-CCM+. Polyhedral grid elements are employed to resolve the majority of the solid and the fluid domain except at the near-wall regions i.e., fluid–solid interface (Figure 3). At these interfaces, four prism layers are used to resolve the velocity and thermal boundary layers and near wall gradients [15,27]. The total number of the generated volume elements in the mesh is 2.7 million for the immersion cooling case and 5.1 million for the cold-plate cooling case.



(**a**) (**b**)

Figure 3. Numerical mesh employed for the numerical simulations of (**a**) immersion cooling, and (**b**) cold-plate cooling.

Table 5. Computational elements in the medium grid for immersion cooling.

Domain	Computational Elements
Li-ion cells	806,347
Coolant	1,641,055
Enclosure	104,367

Table 6. Computational elements in medium grid for cold-plate cooling.

Domain	Computational Elements
Li-ion cells	499,384
Coolant	186,072
Aluminum plate	104,367
Copper tube	4,018,346
Ambient air	165,176

2.7. Numerical Uncertainty Analysis

Uncertainty analysis is an integral part of any numerical simulation as it helps in understanding the accuracy and reliability of the computational results. The process used to quantify numerical uncertainties for the numerical framework employed in the simulations is described in the following two sections. In particular, the uncertainty is divided into two types—namely, grid independence study, and experimental comparison.

2.7.1. Grid Independence Study

The first type of uncertainty estimation is conducted through the use of Grid Convergence Index (GCI) method proposed by Celik et al. [29]. This method has been evaluated and implemented in several hundred CFD studies [30–33]. In order to estimate GCI, Case 3 (Table 4) was simulated on three different grids (Cases 4 & 5), which are shown in Table 7. Solutions obtained from these three grids are compared and the discretization error is then estimated by using the coolant heat transfer coefficient and pressure drop as performance metrics.

Table 7. Computational elements used in the grid independence study performed on the base immersed cooling case.

Grid	Computational Elements	Representative Grid Size
Fine (Case 4)	6,662,613	1.01
Medium (Case 3)	2,738,676	1.37
Coarse (Case 5)	1,229,946	1.78

After conducting simulations on the three grids, the method outlined by Celik et al. [29] is followed to estimate the GCI as shown in Table 8. Here, Ψ_1, Ψ_2, Ψ_3 represent the average coolant heat transfer coefficient (HTC) [in W/m^2K] and maximum cell temperature [in °C] values obtained from each of the three grids, respectively. Relative difference between fine and medium, and medium and coarse grids are represented by $\varepsilon_{21} = (\Psi_2 - \Psi_1)$ and $\varepsilon_{32} = (\Psi_3 - \Psi_2)$. Ψ^{21}_{extra} represents the extrapolated solution of HTC and maximum cell temperature for a grid with representative grid size $\rightarrow 0$. Numerical uncertainties in the fine-grid solution for the HTC and maximum cell temperature are as 0.002% and 1.74%, respectively.

Table 8. Discretization errors from the grid independence study performed on the base immersed cooling case.

Parameter	Average Heat Transfer Coefficient [W/m^{2}K]	Maximum Cell Temperature [°C]
R_{21}	1.35	1.35
R_{32}	1.31	1.31
Ψ_1	240.16	43.78
Ψ_2	239.96	43.63
Ψ_3	232.76	43.84
ε_{21}	−0.20	−0.15
ε_{32}	−7.20	−0.21
p	1.35	0.74
Ψ^{21}_{extra}	240.16	44.4
ε^{21}_{a} [%]	0.08	0.34
ε^{21}_{extra} [%]	0.001	1.37
GCI^{21} [%]	0.002	1.74

2.7.2. Single Cell Experimental Validation

Validation of the presented numerical framework is conducted through comparison of the numerical results with experimental analysis performed at a single-cell level (Figure 4). Two single-cell level CFD simulations and experimental setups are built using a cylindrical 21700 Li-ion cell, one each for the cold-plate and immersion cooling. The simulations are developed using the same strategies as discussed in Section 2.4. Cells used in the setups are instrumented by mounting T-type thermocouples onto their outer surface. Before recording the temperature data using a GRAPHTEC GL840 data logger, the entire sensor assembly (thermocouples affixed to the data logger) is calibrated with a ThermoWorks reference thermometer using a wet calibration procedure involving the use of a water bath

at different temperatures. The reference thermometer has an accuracy of $\pm 0.05\,^{\circ}C$. The total error in the sensor assembly after calibration is in the range of $-0.06\,^{\circ}C$ to $+0.11\,^{\circ}C$. Interested readers can find more information about this study in an article published in [7]. However, for the completeness of this paper, some representative results are shown here.

For this validation exercise, a single cell discharging at a C-rate of $3C$ is considered. The $3D$ numerical results from both immersion and cold-plate cooling strategies are compared with their respective experimental measurements taken using the thermocouples mounted at mid-axial height on the outer surface of the cell can as shown in Figure 4. As can be observed in Figure 5, the study clearly demonstrates a good experimental comparison with a root mean square error (RMSE) $\leq 0.25\,^{\circ}C$. It must be noted that, in the case of a battery module, the temperature of any cell will be thermally impacted by the presence of neighboring heat generating cells. This effect is not captured in the single-cell analysis. However, as far as the accuracy of the numerical framework is concerned, these validation results demonstrate that the numerical methodology consisting of solving the Navier–Stokes and Energy Equations (1)–(10) using a finite volume approach in STAR-CCM+ is capable of accurately estimating the cell temperatures for both cold-plate and immersion cooling strategies.

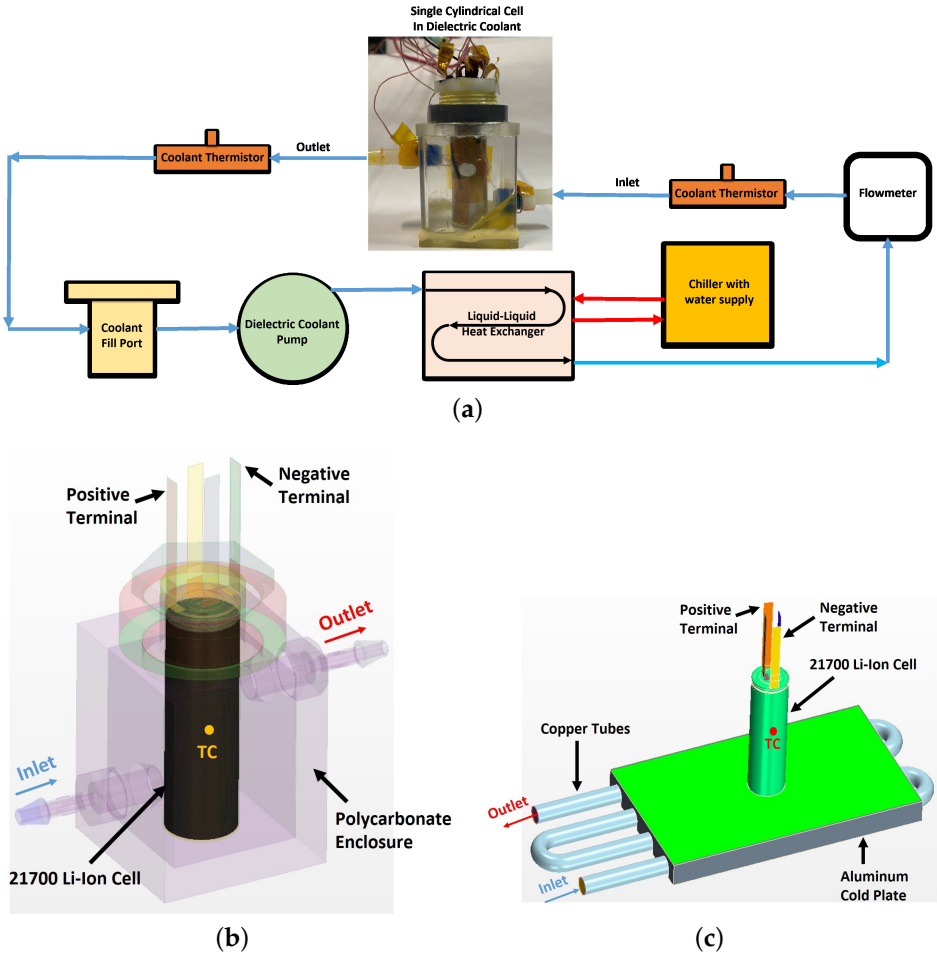


Figure 4. Schematic of the (**a**) overall experimental setup and the geometry employed in [7] for the numerical simulations of (**b**) submerged-cell (immersion) cooling, and (**c**) cold-plate cooling.

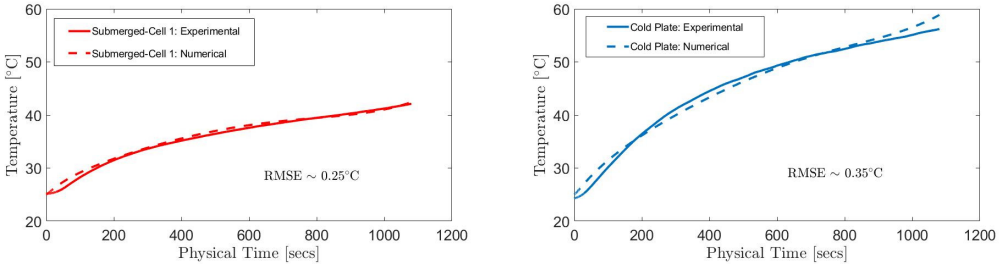


Figure 5. Comparison between experiments and 3D CFD simulations as published in [7] with corresponding root mean square error (RMSE) for, (**a**) immersion cooling, and (**b**) cold-plate cooling.

3. Results and Discussion

3.1. Reference Case Comparison

An overview of flow and thermal behavior of both immersion and cold-plate cooling strategies at the battery module level is discussed in this section. Reference cases used for the direct comparison between the two cooling mechanisms are Case 3 (immersion cooling) and Case 11 (cold-plate cooling), as presented in Table 4.

Figures 6 and 7 show the contours of temperatures at the highlighted cross-sectional planes for immersion-cooled and cold-plate-cooled battery modules, respectively. In the case of immersion-cooled battery module, the dielectric coolant enters the battery module enclosure through the inlet port located at the bottom and exits through the outlet port located at the top of the module towards the opposite end (see Figure 1a). The specific arrangement of cells in the module governs the coolant distribution, which ensures similar coolant temperature distribution along each vertical cross-sectional plane as illustrated by Figure 6a–c. As the coolant moves from the inlet to outlet of the module, heat transfer from the cells results in an increase in its temperature. This subsequently also results in an increase in the temperature of the cells along the direction of the flow towards the outlet of the module.

Figure 7 illustrates the contours of temperature at the end of discharge for a cold-plate-cooled module; temperature distribution on a cross-sectional plane through the middle of the cold-plate and copper tubes as shown in Figure 7a. Heat transfer to the coolant from the base of the cells increases a coolant's temperature as it moves from the inlet to the outlet of the module. In Figure 7a, this is demonstrated by a higher temperature on the cold plate and the coolant regions. This increase in temperature of the coolant influences the temperature distribution of the cells in the battery module resulting in a cluster of hotter cells towards the outlet row of the battery module (Figure 7b). The hottest temperature is demonstrated by the middle cell in the second last row towards the coolant outlet side due to it being surrounded by six neighboring cells. As the corner row cells have fewer neighboring cells, they exhibit relatively lower temperatures compared to their adjacent interior cells.

Figure 8 illustrates the variation of volume-averaged and maximum temperature of the cells in the battery module during the 2C discharge condition for both immersion and cold-plate cooling strategies. In both of these cases, as the module discharges, both average and maximum temperatures of the cells start to increase albeit with different slopes. This is due to the difference in average thermal conductance between the two cooling strategies. A higher thermal conductance in case of the immersion cooling results in early flattening of the temperature curve as compared to the cold-plate based cooling. This is discussed again in Section 3.3. Towards the end of discharge, the cell impedance rapidly increases resulting in a higher heat generation (Figure 2) [34]. This leads to a corresponding rapid increase in the cell temperature. However, the immersion cooling strategy is able to restrict the hottest cell temperature to approximately 44 °C, while the cold-plate-cooled module shows a much higher temperature of 64 °C.

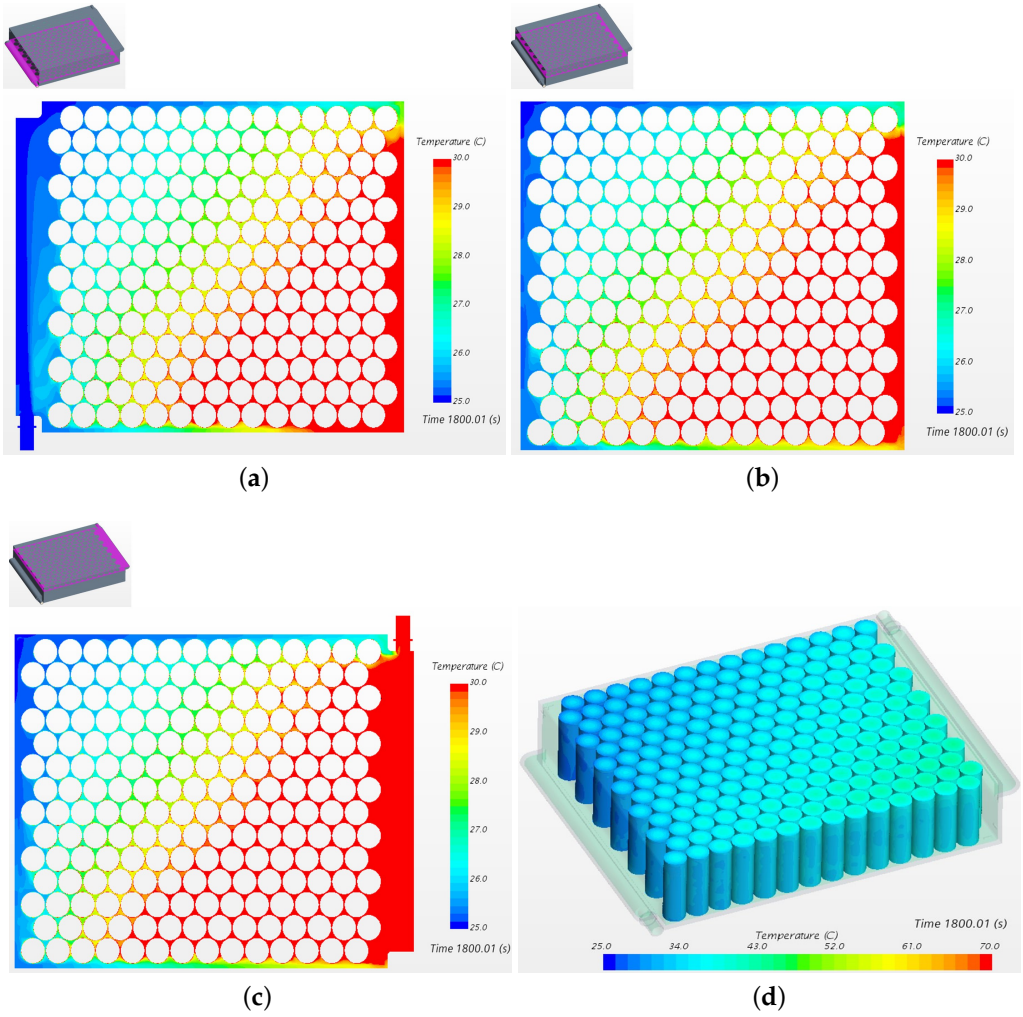


Figure 6. Contours of temperature in (°C) along the cross-sectional vertical plane at Z-height of (**a**) 12 mm, (**b**) 35 mm, and (**c**) 52 mm of the immersion-cooled module. In (**d**), temperature distribution of Li-ion cells within the cold-plate-cooled battery module is shown.

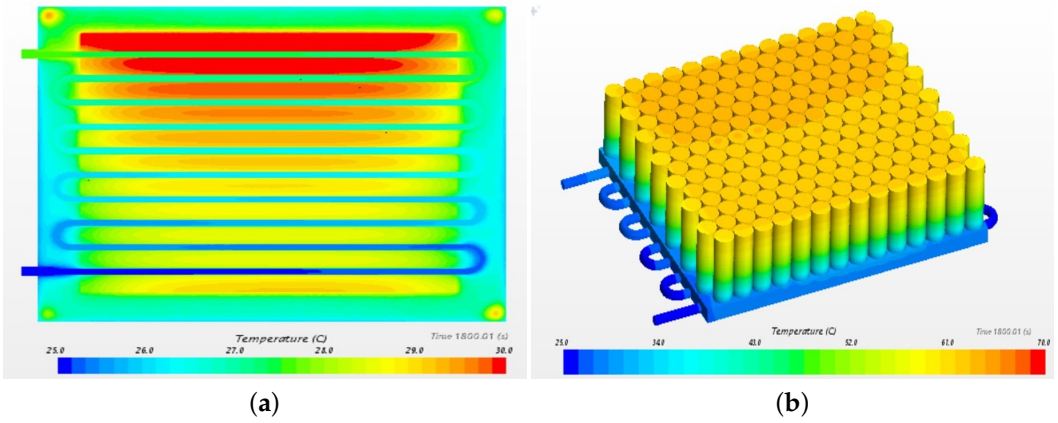
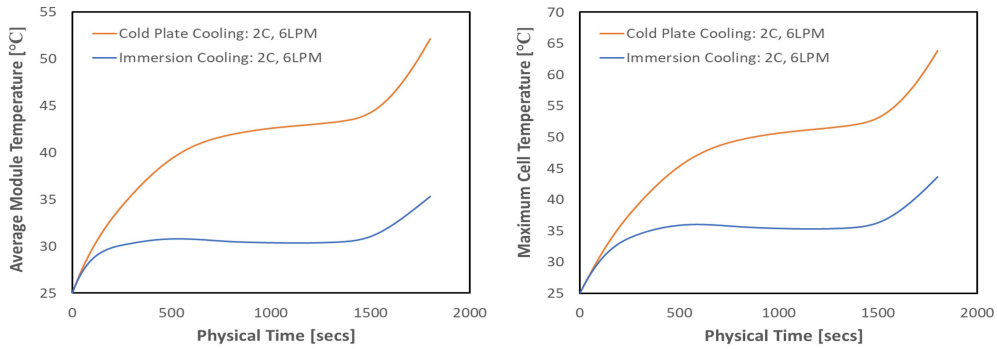


Figure 7. Contours of temperature in (°C) (**a**) along the vertical mid-plane through the cold-plate copper tube, and (**b**) on all the Li-ion cells within the cold-plate-cooled module.

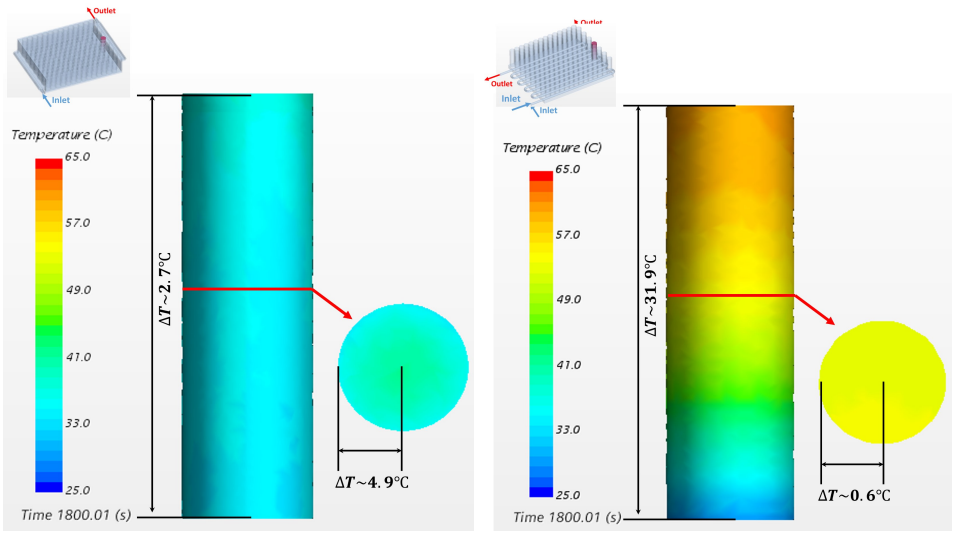
These results for the temperatures clearly show an improved thermal performance with respect to the average and maximum temperatures of the cells in battery module

with dielectric immersion cooling. In terms of thermal gradients within a cell, it can be seen from Figure 9 that a significantly high gradient can develop along the length of the cell in case of cold-plate based cooling. This effect is caused by higher thermal resistance offered by the cell as the heat flows out to the cold plate through the base of the cell. On the other hand, due to transfer of heat from the cell to the dielectric coolant in the radial direction, a higher radial temperature gradient is observed in the case of immersion-cooled cell. It is worth noting, however, that the core cell temperature remains lower for the immersion-cooled cell.



(**a**) (**b**)

Figure 8. Transient behavior of (**a**) average and (**b**) maximum temperatures of all the cells within the battery module.



(**a**) (**b**)

Figure 9. Contours of temperature in (°C) on the outer surface of one Li-ion cell within the module for, (**a**) immersion cooling, and (**b**) cold-plate-cooling.

3.2. Effect of Discharge C-Rate

In this section, the effect of the rate of discharge on module thermal performance is evaluated for cold-plate and immersion cooling strategies. Figure 10a illustrates the variation of maximum cell temperature within the module at the end of discharge with C-rates of 0.5 C, 1 C, 2 C, and 3 C for both cooling methods. Flow rate is kept constant at 6 LPM for this set of simulations. As expected, the highest discharge rate leads to the highest cell temperatures. However, for a lower discharge rate of 0.5 C, the difference in the maximum temperatures between immersion and bottom cold-plate cooling reduces to only 2 °C. The graph indicates that both cooling techniques result in a similar temperature

distribution as the C-rates are reduced further. The lower cost and lower complexity of cold-plate-cooled battery system is preferable under lower C-rate operating conditions.

Figure 10b shows the cell-to-cell temperature differential, as a function of discharge rates, within the immersion-cooled and cold-plate-cooled modules. This is estimated by subtracting the volume average temperatures of the hottest and the coldest cells at the end of each discharge. It can be observed from Figure 10b that the cold-plate-cooled module demonstrates significantly lower cell-to-cell temperature differential at all the considered C-rates when compared to the immersion-cooled module.

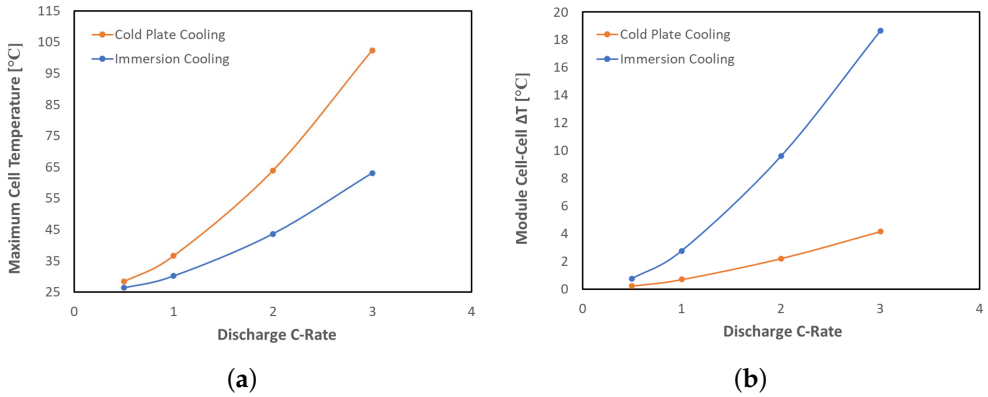


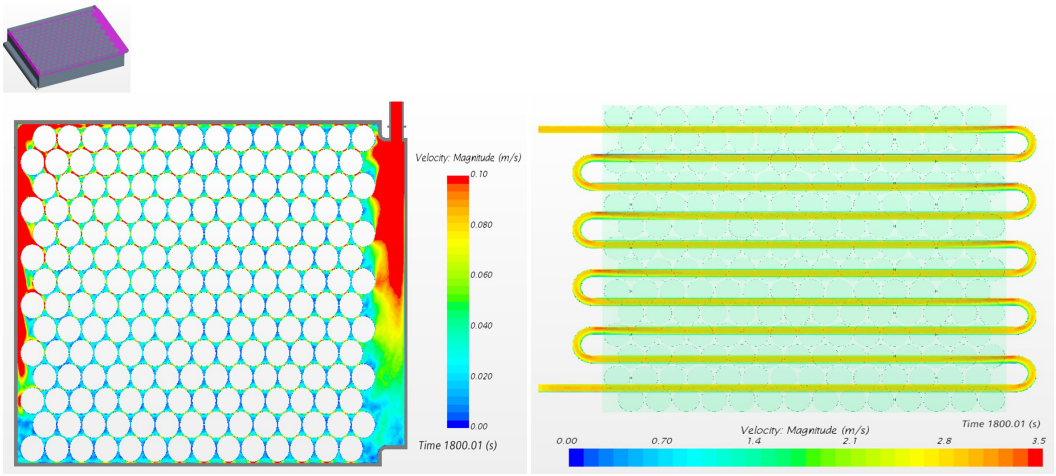
Figure 10. Effect of variation of discharge C-rate on (**a**) maximum cell temperature (°C), and (**b**) cell-to-cell temperature differential within the immersion-cooled and cold-plate-cooled modules (°C).

As ageing of a Li-Ion cell is strongly coupled to its temperature [5–7], an increase in the non-uniformity of cell temperature distribution will result in a larger non-uniform ageing of the cells within the module thereby giving rise to a much wider spectrum of impedance and capacity differences. This causes further non-uniformity in heat generation over the life of the battery and raises operational concerns related to voltage imbalance across different cells within the module [35,36].

The discrepancy in cell-to-cell temperature differential between the two cooling methods is primarily due to a higher heat rejection (Table 9) to the coolant in case of the immersion-cooled module and lower specific heat (Tables 1 and 2) of the dielectric coolant, as compared to WEG 50/50 mixture. Both of these factors cause the overall coolant temperature, and hence the cell temperatures, to increase more in the immersion-cooled module as the coolant flows towards the outlet. It is worth noting that the specific flow passage of the immersion-cooled module also contributes to this higher cell-to-cell temperature differential. This point is further emphasized in Figure 11, where the contours of coolant velocity magnitude are illustrated for both cooling methods. In particular, the serpentine flow path of the coolant with both inlet and outlet ports located on the same side of the cold-plate, in conjunction with the heat spreading capability of the aluminum cold-plate, contributes to a relatively better homogenization of the cell temperatures across the entire module albeit with significantly higher maximum and average cell temperatures. On the other hand, the coolant path inside immersion-cooled module is the result of the specific cell arrangement and the outlet port location. As can be observed in Figure 11a, the coolant path for the relatively simplistic immersion-cooled module design considered in this study creates regions of low velocity, which then leads to higher cell temperature along the outlet manifold away from the outlet port.

Table 9. Variation of heat rejection to the coolant and coolant temperature rise at the end of discharge at different module discharge rates.

Discharge Rate	Heat Rejection from Cells [W]		Coolant Temperature Rise [°C]	
	Immersion Cooling	Cold-Plate Cooling	Immersion Cooling	Cold-Plate Cooling
0.5 C	82.59	74.72	0.46	0.23
1 C	317.30	265.77	1.75	0.75
2 C	1173.69	919.59	6.38	2.52
3 C	2475.17	1868.46	13.29	5.14



(**a**) (**b**)

Figure 11. Contours of coolant velocity magnitude in (m/s) along (**a**) the exit plane within the immersion-cooled module, and (**b**) the vertical mid-plane through the cold-plate copper tube.

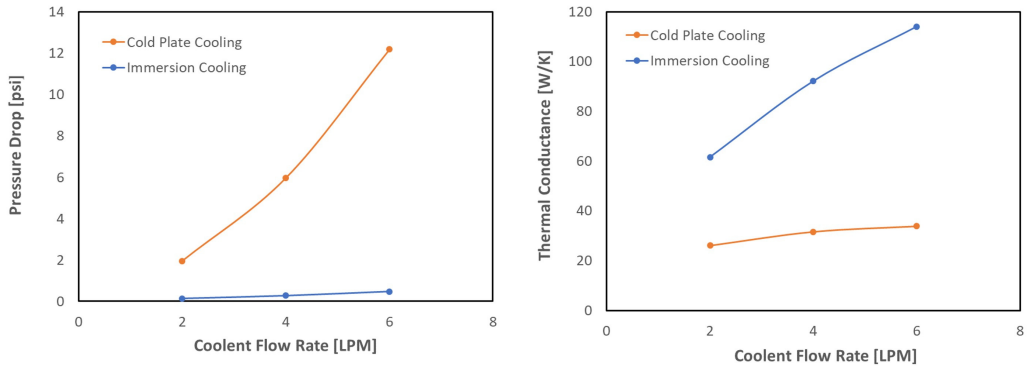
3.3. Effect of Coolant Flow Rate

This section presents the effect of the coolant flow rate on the module thermal performance is evaluated for immersion-cooled and cold-plate-cooled battery modules. The numerical simulations are performed for each cooling method at three different coolant flow rates- 2 LPM, 4 LPM, and 6 LPM.

Coolant pressure drop plays a significant role in the design of any battery module cooling system. As shown in Figure 12a, as coolant flow rate increases, the pressure drop increases nonlinearly for both cooling systems. However, the pressure drop is significantly higher for the cold-plate-cooled module as compared to the immersion-cooled module. Lower viscosity and density of the dielectric fluid coupled with a parallel flow distribution inside the immersion-cooled module results in this behavior. As pumping power is directly proportional to the pressure drop, the results imply that, for the same pumping power, a much higher flow rate can be provided to the immersion-cooled module, as compared to the cold-plate-cooled module.

A higher coolant flow rate is expected to enhance the convective heat transfer, thereby lowering the cell temperatures. In order to quantify and compare this effect for both the cooling methods, thermal conductance (in W/K), which is the product of the heat transfer coefficient and the heat transfer area, is used as a performance metric. Specifically, this parameter is computed through the heat transfer to the coolant (W), and volume averaged temperature rise of all the cells in the module at the end of discharge. As shown in Figure 12b, thermal conductance for both the modules increases with increasing coolant flow rate. This is due to the fact that an increase in flow velocities around the cells and the coolant channels results in an increase in the average and local heat transfer coefficients. Based on the slope of the curves, it can be noted, in the case of a cold-plate-

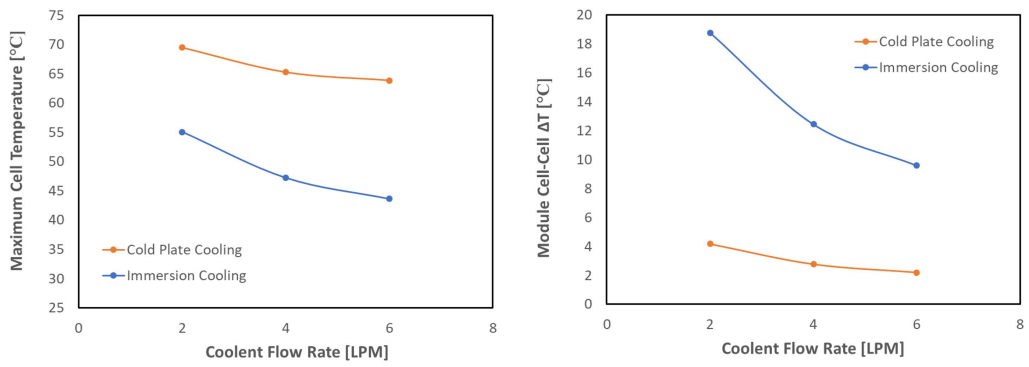
cooled module, that any further increase in flow rates may eventually result in a flattening out of the thermal conductance curve. Furthermore, in the case of immersion cooling, a much larger cell surface area participates in the heat transfer process to the coolant leading to a significantly higher thermal conductance for the immersion-cooled module compared to the cold-plate-cooled module.



(**a**) (**b**)

Figure 12. Effect of variation of flow rate on (**a**) coolant pressure drop (psi), and (**b**) average thermal conductance (W/K).

Figure 13a shows the variation of maximum cell temperatures within the module for both cooling strategies. It can be observed from the results that, with an increase in the coolant flow rate, the maximum cell temperature decreases for both of the systems due to the increase in coolant heat transfer coefficient. Figure 13b shows the cell-to-cell temperature differential, as a function of coolant flow rates, within the immersion-cooled and cold-plate-cooled modules. Like Figure 10b, this is estimated by subtracting the volume average temperatures of the hottest and the coldest cells at the end of each discharge. Results show that, as the flow rate increases, the cell-to-cell temperature differential decreases for both the modules. It should be noted that for immersion cooling a higher cell-to-cell temperature differential is the outcome of the specific flow distribution, as pointed out in Figure 11a, a higher heat rejection from cells to the coolant and the lower specific heat of the dielectric coolant as compared to 50/50 EG-water mixture employed in the cold-plate cooling. Providing a higher coolant flow rate at the inlet of the module can help in alleviating this higher cell-to-cell temperature differential. Owing to a much lower pressure drop across the immersion-cooled module (Figure 12a), this can be achieved without spending considerably higher pumping power across the module.



(**a**) (**b**)

Figure 13. Effect of variation of coolant flow rate on (**a**) maximum cell temperature (°C), and (**b**) cell-to-cell temperature differential within the immersion-cooled and cold-plate-cooled modules (°C).

3.4. Additional Discussion and Future Work

In addition to the results presented in the previous sections, another distinct advantage of immersion cooling is increased safety, especially in the event of a coolant leakage or an accident. As cold-plate cooling involves the use of 50/50 EG/water, any leakage near the electrical components or cells can result in a safety hazard, such as an electrical short circuit, due to the coolant's high electrical conductivity. On the other hand, the dielectric nature of the coolant in an immersion-cooled battery module provides an additional layer of safety during such occurrences.

In spite of these inherent advantages, there are some challenges associated with the practical implementation of immersion cooling in a battery module. Specifically, material selection for the entire cooling system must consider compatibility of its constituent components with the dielectric liquid. This includes vehicle level cooling lines and systems as well. This is particularly challenging as there are relatively fewer commercially available plastics, rubbers, and seals that are compatible with dielectric liquids, as compared to a WEG 50/50 mixture. For example, the dielectric liquid considered in this work is compatible with elastomeric materials that contain a low amount of plasticizers [24]. This limits the pool of materials that a battery module designer can essentially select from.

Finally, one of the main thermal performance related issues for immersion cooling that has been observed in the current study is a higher cell-to-cell temperature differential within the battery module. Thus, our future work will involve studying mechanisms to mitigate this non-uniformity in the temperature distribution within the immersion-cooled battery module through flow path optimization, varying coolant flow rates, and use of different dielectric coolants. Moreover, the effect of electrical circuitry (collectors, busbars, etc.) and other components on the cell temperatures will also be included in any future effort.

4. Conclusions

Thermal performance of immersion cooling in an NCA-chemistry based cylindrical 21700 Li-ion battery module was successfully evaluated and compared directly with a more prevalent cold-plate based cooling strategy. For both cooling mechanisms, the effect of module discharge C-rate and coolant flow rate on coolant pressure drop, maximum cell temperature, cell-to-cell temperature differential, and thermal conductance was analyzed by performing parametric 3*D* CFD simulations using an experimentally validated numerical methodology. Results from the numerical analyses at different module C-rates (0.5 C, 1 C, 2 C, and 3 C) showed that, at higher C-rates, an immersion-cooled battery module shows significantly lower maximum and average battery temperatures as compared to the cold-plate-cooled module. However, the difference between the two cooling strategies was considerably reduced at lower C-rates. This was evident from the results for the discharge at 0.5 C, which showed that the difference in the maximum cell temperature between the two modules is reduced to less than 2 °C implying that both cooling strategies will result in a similar thermal performance at lower module C-rates. In terms of the temperature distribution across the module, the cold-plate-cooled battery module showed much better homogeneity. Owing to a higher rate of heat transfer and lower thermal properties of the dielectric liquid, the overall cell-to-cell temperature differential was observed to be higher in the case of an immersion-cooled battery module. Based on the analyses at different coolant flow rates (2 LPM, 4 LPM, and 6 LPM), it was observed that the thermal conductance for immersion cooling was around 2.5–3 times higher than the cold-plate cooling for the considered coolant flow rates. Thermal conductance increased with increasing flow rates for both cooling configurations and showed the potential to increase further in case of immersion cooling with higher flow rates. Moreover, for all considered coolant flow rates, the observed pressure drop was 15–25 times higher for the cold-plate-cooled module as compared to an immersion-cooled module. Due to such a low pressure drop for the immersion-cooled module, it is possible to increase its thermal performance further by providing a higher flow rate at the module inlet for the same pumping work

as compared to the cold-plate-cooled module. This will also reduce the higher cell-to-cell temperature differential observed in the case of the immersion-cooled battery module. Overall, it was evident from the results of this study that, based on the considered metrics, that immersion cooling strategy provides an improved thermal performance for EV battery modules operating under aggressive C-rates or duty cycles. The only exception to this is the temperature uniformity or cell-to-cell temperature differential across the modules that was observed to be much better in case of the cold-plate based cooled module.

Author Contributions: All authors have worked on this manuscript together and all authors have read and agreed to the published version of the manuscript. Conceptualization, P.D., G.P. and A.K.S.; methodology, P.D. and G.P.; software, P.D. and G.P.; validation, P.D. and G.P.; formal analysis, P.D. and G.P.; investigation, P.D. and G.P.; resources, P.D. and G.P.; data curation, P.D., G.P. and A.K.S.; writing—original draft preparation, P.D. and G.P.; writing—review and editing, P.D., G.P. and A.K.S.; visualization, P.D., G.P. and A.K.S.; supervision, P.D. and A.K.S.; project administration, A.K.S.

Funding: This research received no external funding.

Institutional Review Board Statement: Not applicable.

Informed Consent Statement: Not applicable.

Data Availability Statement: Not applicable.

Acknowledgments: We extend our gratitude to Romeo Power Technology for making this work possible. Our appreciations also go out to Shashwat Bakhshi for his support on CAD preparation.

Conflicts of Interest: The authors declare no conflict of interest.

References

1. Ma, Y.; Shi, T.; Zhang, W.; Hao, Y.; Huang, J.; Lin, Y. Comprehensive policy evaluation of NEV development in China, Japan, the United States, and Germany based on the AHP-EW model. *J. Clean. Prod.* **2019**, *214*, 389–402. [CrossRef]
2. IEA. *Global EV Outlook 2020*; International Energy Agency: Paris, France, 2020
3. Bryden, T.S.; Hilton, G.; Dimitrov, B.; de León, C.P.; Cruden, A. Rating a stationary energy storage system within a fast electric vehicle charging station considering user waiting times. *IEEE Trans. Transp. Electrif.* **2019**, *5*, 879–889. [CrossRef]
4. Feng, X.; Zheng, S.; Ren, D.; He, X.; Wang, L.; Cui, H.; Liu, X.; Jin, C.; Zhang, F.; Xu, C.; et al. Investigating the thermal runaway mechanisms of lithium-ion batteries based on thermal analysis database. *Appl. Energy* **2019**, *246*, 53–64. [CrossRef]
5. Lu, L.; Han, X.; Li, J.; Hua, J.; Ouyang, M. A Review on the Key Issues for Lithium-Ion Battery Management in Electric Vehicles. *J. Power Sources* **2013**, *226*, 272–288. [CrossRef]
6. Leng, F.; Tan, C.M.; Pecht, M. Effect of temperature on the aging rate of Li ion battery operating above room temperature. *Sci. Rep.* **2015**, *5*, 1–12. [CrossRef] [PubMed]
7. Pulugundla, G.; Dubey, P.; Wu, Z.; Wang, Q.; Srouji, A.K. Thermal Management of Lithium Ion Cells at High Discharge Rate using Submerged-Cell Cooling. In Proceedings of the 2020 IEEE Transportation Electrification Conference Expo (ITEC), Chicago, IL, USA, 23–26 June 2020; pp. 1–5.
8. Kellner, Q.; Worwood, D.; Widanage, W.D.; Marco, J. Electrical and thermal behavior of pouch-format lithium ion battery cells under high-performance and standard automotive duty-cycles. In Proceedings of the IEEE Vehicle Power and Propulsion Conference (VPPC), Belfort, France, 11–14 December 2017; pp. 1–5.
9. Worwood, D.; Hosseinzadeh, E.; Kellner, Q.; Marco, J.; Greenwood, D.; McGlen, R.; Widanage, W.D.; Barai, A.; Jennings, P. Thermal analysis of a lithium-ion pouch cell under aggressive automotive duty cycles with minimal cooling. In Proceedings of the 6th Hybrid and Electric Vehicles Conference (HEVC), London, UK, 2–3 November 2016; pp. 1–6.
10. Pesaran, A.A.; Markel, T.; Tataria, H.S.; Howell, D. *Battery Requirements for Plug-In Hybrid Electric Vehicles—Analysis and Rationale*; No. NREL/CP-540-42240; National Renewable Energy Lab. (NREL): Golden, CO, USA, 2009.
11. Marano, V.; Onori, S.; Guezennec, Y.; Rizzoni, G.; Madella, N. Lithium-ion batteries life estimation for plug-in hybrid electric vehicles. In Proceedings of the IEEE Vehicle Power and Propulsion Conference, Dearborn, MI, USA, 7–10 September 2009; pp. 536–543.
12. Troxler, Y.; Wu, B.; Marinescu, M.; Yufit, V.; Patel, Y.; Marquis, A.J.; Brandon, N.P.; Offer, G.J. Effect of temperature on the aging rate of Li ion battery operating above room temperature. *J. Power Sources* **2014**, *247*, 1018–1025. [CrossRef]
13. Yang, N.; Zhang, X.; Shang, B.; Li, G. Unbalanced discharging and aging due to temperature differences among the cells in a lithium-ion battery pack with parallel combination. *J. Power Sources* **2016**, *306*, 733–741. [CrossRef]
14. Fleckenstein, M.; Bohlen, O.; Roscher, M.A.; Bäker, B. Current density and state of charge inhomogeneities in Li-ion battery cells with LiFePO4 as cathode material due to temperature gradients. *J. Power Sources* **2011**, *196*, 4769–4778. [CrossRef]

15. Pulugundla, G.; Dubey, P.; Srouji, A. *Time-Accurate CFD Analysis of Liquid Cold Plates for Efficient Thermal Performance of Electric Vehicle Li-Ion Battery Modules*; SAE Technical Paper; SAE International: Warrendale, PA, USA, 2019
16. Bakhshi, S.; Dubey, P.; Wu, Z.; Srouji, A.K. Comparison of different liquid cooling configurations for effective thermal management of li-ion pouch cell for automotive applications. In Proceedings of the ASME Heat Transfer Summer Conference, Orlando, FL, USA, 12–15 July 2020.
17. Porter, W.P.; Ashraf, U.; Thibault, R.W.; Certo, N.; Dubey, P.; Galvan, K. Cold Plate Blade for Battery Modules. U.S. Patent 16/357,170, 19 September 2019.
18. Hermann, W.A. Liquid Cooling Manifold with Multi-Function Thermal Interface. U.S. Patent 8,263,250, 11 September 2019.
19. Kim, G.H.; Pesaran, A. Battery Thermal Management Design Modeling. *World Electr. Veh. Assoc. J.* **2007**, *1*, 126–133. [CrossRef]
20. Patil, M.S.; Seo, J.H.; Bang, Y.M.; Kim, D.W.; Ekanayake, G.; Singh, G.; Kim, H.M.; Choi, Y.H.; Lee, M.Y. A Novel Design for Lithium-Ion Battery Cooling using Mineral Oil. *Adv. Sci. Technol. Lett.* **2016**, *141*, 164–168.
21. Deng, Y.; Feng, C.; E, J.; Zhu, H.; Chen, J.; Wen, M.; Yin, H. Effects of different coolants and cooling strategies on the cooling performance of the power lithium ion battery system: A review. *Appl. Therm. Eng.* **2018**, *142*, 10–29. [CrossRef]
22. Sundin, D.W.; Sponholtz, S. Thermal Management of Li-Ion Batteries With Single-Phase Liquid Immersion Cooling. *IEEE Open J. Veh. Technol.* **2020**, *1*, 82–92. [CrossRef]
23. Patil, M.S.; Seo, J.H.; Lee, M.Y. A Novel Dielectric Fluid Immersion Cooling Technology for Li-ion Battery Thermal Management. *Energy Convers. Manag.* **2021**, *229*, 113715. [CrossRef]
24. 3M™ Novec™7500 Engineered Fluid. Available online: https://multimedia.3m.com/mws/media/65496O/3m-novec-7500-engineered-fluid.pdf (accessed on 1 April 2020).
25. Islam, M.R.; Shabani, B.; Rosengarten, G. Electrical and Thermal Conductivities of 50/50 Water-ethylene Glycol Based TiO2 Nanofluids to be Used as Coolants in PEM Fuel Cells. *Energy Procedia* **2017**, *110*, 101–108. [CrossRef]
26. Engineering ToolBox. Available online: https://www.engineeringtoolbox.com (accessed on 1 April 2020).
27. STAR-CCM+ User Manual. Available online: http://www.cd-adapco.com/products/star-ccm/documentation (accessed on 1 April 2020)
28. Patankar, S.V.; Spalding, D.B. A calculation procedure for heat, mass and momentum transfer in three-dimensional parabolic flows. *J. Heat Mass Tran.* **1972**, *15*, 1787–1806. [CrossRef]
29. Celik, I.B.; Ghia, U.; Roache, P.J.; Freitas, C.J.; Coleman, H.; Raad, P.E. Procedure for estimation and reporting of uncertainty due to discretization in CFD applications. *J. Fluids Eng.* **2008**, *130*, 078001.
30. Dubey, P.; Ghia, U.; Turkevich, L.A. Computational fluid dynamics analysis of the Venturi Dustiness Tester. *Powder Technol.* **2017**, *312*, 310–320. [CrossRef] [PubMed]
31. Xing, Y.; Spring, S.; Weigand, B. Experimental and numerical investigation of impingement heat transfer on a flat and micro-rib roughened plate with different crossflow schemes. *Int. J. Therm. Sci.* **2011**, *50*, 1293–1307. [CrossRef]
32. Promvonge, P.; Jedsadaratanachai, W.; Kwankaomeng, S. Numerical study of laminar flow and heat transfer in square channel with 30 inline angled baffle turbulators. *Appl. Therm. Eng.* **2010**, *30*, 1292–1303. [CrossRef]
33. Dubey, P.; Ghia, U.; Turkevich, L.A. Numerical investigation of sheath and aerosol flows in the flow combination section of a baron fiber classifier. *Aerosol Sci. Technol.* **2014**, *48*, 896–905. [CrossRef] [PubMed]
34. Cho, I.H.; Lee, P.Y.; Kim, J.H. Analysis of the Effect of the Variable Charging Current Control Method on Cycle Life of Li-ion Batteries. *Energies* **2019**, *12*, 3023. [CrossRef]
35. Barsukov, Y. *Battery Cell Balancing: What to Balance and How*; Texas Instruments: Dallas, TX, USA, 2006; p. 2.
36. Qi, J.; Lu, D.D.C. Review of battery cell balancing techniques. In Proceedings of the 2014 Australasian Universities Power Engineering Conference (AUPEC), Perth, WA, Australia, 28 September–1 October 2014; pp. 1–6.